

# Frequency and Bandwidth Design of FR3-Band Acoustic Filters

Taran Anusorn, *Student Member, IEEE*, Omar Barrera, *Student Member, IEEE*, Jack Kramer, *Student Member, IEEE*, Ian Anderson, *Student Member, IEEE*, Ziqian Yao, *Student Member, IEEE*, Vakhtang Chulukhadze, *Student Member, IEEE*, and Ruochen Lu, *Senior Member IEEE*

**Abstract**—This article presents an approach to control the operating frequency and fractional bandwidth (FBW) of miniature acoustic filters in thin-film lithium niobate (TFLN). More specifically, we used the first-order antisymmetric mode in first-order antisymmetric (A1) mode lateral-field-excited bulk acoustic wave resonators (XBARS) to achieve efficient operation at 20.5 GHz. Our technique leverages the thickness-dependent resonance frequency of A1 XBARS, combined with the in-plane anisotropic properties of 128° Y-cut TFLN, to customize filter characteristics. The implemented three-element ladder filter prototype achieves an insertion loss (IL) of only 1.79 dB and a controlled 3-dB FBW of 8.58% at 20.5 GHz, with an out-of-band (OoB) rejection greater than 14.9 dB across the entire FR3 band, while featuring a compact footprint of  $0.90 \times 0.74 \text{ mm}^2$ . Moreover, an eight-element filter prototype shows an IL of 3.80 dB, an FBW of 6.12% at 22.0 GHz, and a high OoB rejection of 22.97 dB, demonstrating the potential for expanding to higher-order filters. As frequency allocation requirements become more stringent in future FR3 bands, our technique showcases promising capability in enabling compact and monolithic filter banks toward next-generation acoustic filters for 6G and beyond.

**Index Terms**—Acoustic devices, filters, FR3, lithium niobate, microelectromechanical systems (MEMS), piezoelectricity.

## I. INTRODUCTION

**F**REQUENCY RANGE 3 (FR3), spanning from 7.125 GHz to 24.25 GHz, is emerging as a key spectrum solution for 6G and beyond [1]–[3]. It offers a favorable balance between spectral efficiency, coverage, and deployment cost [2]–[5]. Despite not being finalized yet, the bandwidth (BW) of the FR3 frequency bands is expected to vary from 100 MHz to over 2.5 GHz [6], [7], for the coexistence of multiple standards and services within this spectrum. Thus, precise bandpass filter (BPF) design is essential to minimize interference. While integrated passive device (IPD) filters offer a chip-scale footprint, their moderate roll-off limits the frequency selectivity [8]. Conventional distributed microwave filters, such as waveguides and microstrip patches, can be designed to meet passband specifications [9], [10], but their footprint is relatively large for handheld devices, intrinsically limited by electromagnetic (EM) wavelengths (e.g., wavelength  $\lambda \sim 2 \text{ cm}$  at 15 GHz). This fact limits their utilization in commercial

mobile applications. Several advanced efforts, such as defected ground structures (DGSs) in a printed circuit board (PCB) [11], [12] and slow-wave structures realized by either substrate integrated waveguide (SIW) in a PCB [13], [14], through-silicon via (TSV) technique [15], through-glass via (TGV) technique [16], [17], or low-temperature co-fired ceramic (LTCC) technology [18], [19], have been presented with smaller footprints. While these methods achieve significant miniaturization to sub-wavelength scales, their further miniaturization is ultimately still limited by EM wavelengths. To overcome such limits, acoustic wave filters—possessing wavelengths four to five orders of magnitude shorter than their EM counterparts [20]—hold great promise in enabling chip-scale microwave microsystems [21].

For the past decades, acoustic filters have been dominant mobile filter solutions below 6 GHz owing to their exceptionally low insertion loss (IL) and wide bandwidth (BW) within a compact footprint [22]. These filters consist of a network of acoustic resonators that convert EM signals into mechanical vibrations and back via the piezoelectric effect [23]. Below 3 GHz, surface acoustic wave (SAW) resonators are commonly used, where standing waves are confined to the surface of a piezoelectric material [24]. The operating frequency ( $f_c$ ) of SAW filters is primarily determined by the lateral distance between the interdigital electrodes (IDEs) of their resonators. However, this design feature limits the operation at high frequencies, as the IDE pitch widths become exceedingly small, causing resistive loss and fabrication challenges [25]. In contrast, bulk acoustic wave (BAW) resonators, which vibrate throughout their acoustic cavity body [26], offer better scalability by reducing the piezoelectric and metal stack thickness. Nevertheless, ultra-thin films inherently suffer from higher losses, limiting BAW filter development below 10 GHz [27]. Recent advancements have improved the performance of film bulk acoustic resonators (FBARs) [28]–[31], making them more viable, particularly in the FR3 band, but they still suffer from issues originating from thin top and bottom electrode layers.

First-order antisymmetric (A1) Lamb mode lateral-field-excited bulk acoustic wave resonators (XBARS) in thin-film lithium niobate (TFLN) [32]–[34] arise as one promising high-frequency acoustic filter platform [35]. Owing to the high quality factor ( $Q$ ) and notably strong electromechanical coupling ( $k^2$ ) [36], low-loss acoustic filters beyond 20 GHz with a wide fractional bandwidth (FBW) of up to 19.8% have been realized recently using A1 XBARS in 128° Y-cut TFLN [37]–

This work was supported in part by DARPA COFFEE project and in part by Anandamahidol Foundation Scholarship. This article is an expanded version from the IEEE International Microwave Symposium, June 2025. (Corresponding author: Taran Anusorn).

The authors are with the Department of Electrical and Computing Engineering, The University of Texas at Austin, Austin, TX 78712 USA (e-mail: taran.anusorn@utexas.edu).

[39]. Nevertheless, a wide FBW is not always an ideal solution, as 6G FR3 requires a specific FBW to match the allocated band. To address this, we leverage the anisotropic material properties of 128° Y-cut TFLN to fine-tune  $k^2$  of the A1 XBAR by simply rotating its IDEs. This approach enables the customization of resonator properties, namely, resonance ( $f_s$ ) and  $k^2$ , allowing for synthesizing acoustic filters of various specifications without adding excessive design complexity and fabrication/integration process.

In this work, to validate the technique, we designed and fabricated A1 XBAR ladder filter prototypes targeting FR3 operation with a controlled FBW below 10%. The three-element prototype, with an FBW of 8.58%, achieves a low IL of 1.79 dB and an out-of-band (OoB) rejection level exceeding 14.92 dB across the entire FR3 band, all while maintaining a compact footprint of only  $0.90 \times 0.74 \text{ mm}^2$ . Moreover, our 8-element prototype yields an FBW of 6.12% with a better minimum OoB rejection of 22.97 dB at the cost of a slightly higher IL of 3.80 dB, showcasing the potential for higher-order filter design. Compared to previously reported FR3 acoustic filters above 10 GHz [38]–[43], as well as other advanced filter technologies, our results demonstrate exceptional filter performance and unprecedented design controllability, opening doors toward a precise and flexible design of next-generation acoustic filters.

This article is an extension of [1], which briefly reported preliminary demonstration of frequency and bandwidth of acoustic filters, but here we have a different set of resonator designs, filter implementations, experimental data, and a more detailed design methodology of TFLN XBAR-based acoustic filters. The paper is organized as follows. Section II introduces the principles of acoustic filter design, highlighting important aspects of controlling filter characteristics through the properties of acoustic resonators. Section III presents a finite element analysis (FEA) of rotating A1 XBAR for  $k^2$  tuning. Section IV provides a detailed description of the proposed design approach with filter simulation. Section V presents and discusses the measurement results of our fabricated devices. Finally, Section VI states the conclusion.

## II. PRINCIPLES OF ACOUSTIC FILTER DESIGN

Designing acoustic filters requires a fundamental understanding of the working mechanisms of an acoustic resonator. When an electrical signal passes through the resonator, the piezoelectric effect converts it into mechanical vibrations, which resonate at specific frequencies. This transduction process appears as admittance antiresonance, as illustrated in Fig. 1(a), where series resonance ( $f_s$ ) corresponds to high admittance, while parallel resonance ( $f_p$ ) represents low admittance. Key figures of merit (FoMs) of the resonator include  $Q$  and  $k^2$ , which represent energy dissipation and the efficiency of energy conversion between the electrical and mechanical domains, respectively.  $Q$  is defined as a ratio of resonant frequency and a 3-dB bandwidth of the resonance, while  $k^2$  is given by [44]:

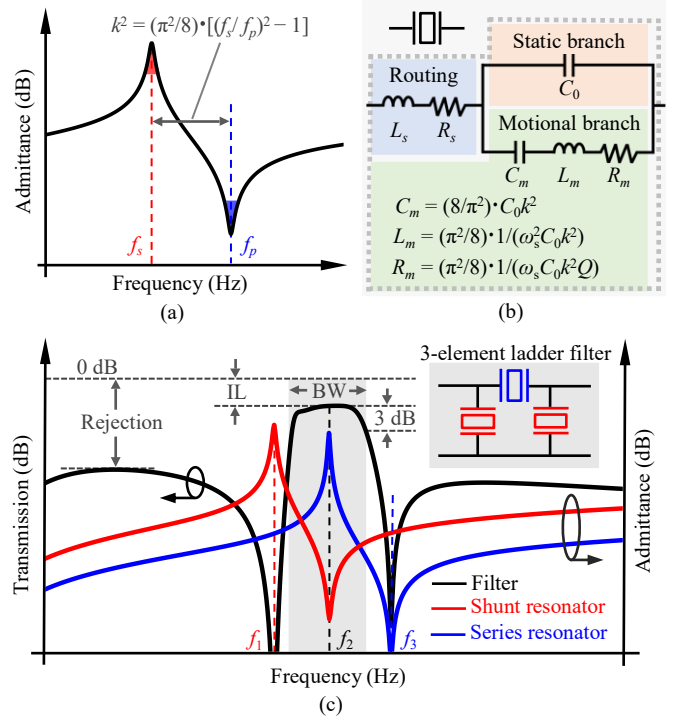


**Fig. 1.** Important components of acoustic filters. (a) Admittance characteristics over frequency of a generic acoustic resonator. (b) mBVD resonator model. (c) Transmission characteristics of a three-element ladder acoustic filter along with the admittance of the resonators.

$$k^2 = (\pi^2/8) \cdot [(f_p/f_s)^2 - 1]. \quad (1)$$

The modified Butterworth-Van Dyke (mBVD) model [45], shown in Fig. 1(b), accurately captures the electrical behavior of the acoustic resonator. The static capacitance ( $C_0$ ) of a resonator is set by the dimensions and the dielectric stack between IDE. Meanwhile, the motional branch, consisting of the motional capacitance ( $C_m$ ), motional inductance ( $L_m$ ), and motional resistance ( $R_m$ ), directly corresponds to the electromechanical transduction. These parameters are defined as:

$$C_m = (8/\pi^2) \cdot C_0 k^2, \quad (2)$$

$$L_m = (\pi^2/8) \cdot 1/(\omega_s^2 C_0 k^2), \quad (3)$$

$$R_m = (\pi^2/8) \cdot 1/(\omega_s C_0 k^2 Q), \quad (4)$$

where  $\omega_s = 2\pi f_s$ .

In addition to the two branches representing the active region, the mBVD model incorporates the effects of routing elements, such as probing pads and buslines, by including a series inductance ( $L_s$ ) and resistance ( $R_s$ ). The impact of  $L_s$  and  $R_s$  on the acoustic filters will be discussed later in Section V.

To build intuition around acoustic filter design, Fig. 1(c) illustrates the transmission characteristics of a three-element ladder acoustic filter, comprising one series and two shunt resonators, alongside the admittance profiles of its resonators. At frequency  $f_1$ , the shunt resonators exhibit high admittance, essentially acting as grounds at both ports, which results in a transmission zero (TZ). At frequency  $f_2$ , the series resonator exhibits maximum admittance, while the shunt resonators have minimum admittance, enabling effective signal transmission

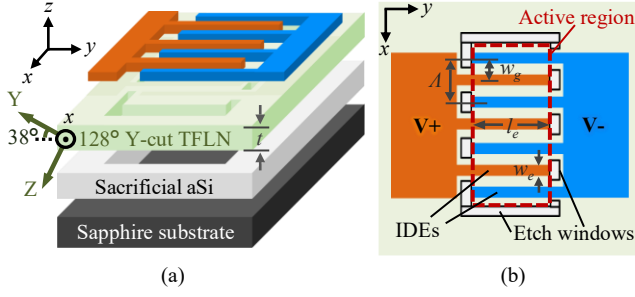


Fig. 2. (a) Exploded and (b) top views of the A1 XBAR in 128° Y-cut TFLN.

through the filter. The IL of the filters is therefore influenced by  $Q$  and  $R_s$  of the resonators. Moreover, the filter's  $f_c$  can be approximated from  $f_s$  of the series resonator. Moving to frequency  $f_3$ , another TZ is created by  $f_p$  of the series resonator. Since the bandwidth (BW) of the filter must lie between these two TZs, determined by  $k^2$  of both resonators, FBW can be directly tailored through resonator design.

### III. FIRST-ORDER ANTISYMMETRIC MODE RESONATORS

Since the performance of acoustic filters is closely tied to the properties of their constituent resonators, this section provides a comprehensive background on A1 XBARS in 128° Y-cut TFLN in the proposed filter design.

#### A. First-Order Antisymmetric Lamb Mode Device

A generic XBAR consists of IDE structures fabricated on top of a suspended thin-film piezoelectric layer (e.g., 128° Y-cut TFLN with thickness  $t$ ), as shown in Fig. 2(a). The material axes  $X$ ,  $Y$ ,  $Z$  will be explained later in this section. To achieve suspension, a sacrificial layer, commonly made of chemically removable materials such as amorphous silicon (aSi), is deposited between the film and a substrate. As shown in Fig. 2(b), etch windows are used to release the thin film and also to define the active region of the resonator. Placing the buslines outside this active region helps prevent the generation of spurious modes and minimizes feedthrough capacitance between the buslines [35]. The dimensions of IDEs, including electrode width  $w_e$  and gap width  $w_g$ , should be chosen to achieve a desirable trade-off between  $Q$  and  $k^2$  [35].

In this work, we used  $w_e = 2.2 \mu\text{m}$  and  $w_g = 0.8 \mu\text{m}$ , which corresponds to a periodicity of  $A = 2(w_e + w_g) = 6 \mu\text{m}$ . When an alternating voltage is applied to the IDEs, an electric field (E-field) is generated between each IDE pair and laterally excites mechanical vibrations through the piezoelectric effect. Unlike SAW devices, where the wavelength of the laterally excited acoustic wave is determined by the IDE periodicity  $A$ , XBARS support a standing BAW, which is dominantly confined within the suspended film by the mechanically free boundaries at both the top and bottom surfaces (i.e., air interfaces). It is worth noting that the width  $w_e$  has minimal impact on the electromechanical transduction in XBARS, as long as  $w_e$  is significantly larger than the film thickness. Moreover, the IDE length  $l_e$  and the number of IDE fingers  $N$  only affect  $C_0$  of the XBARS.

Acoustic modes can be classified based on their dominant stress components when the film thickness is significantly

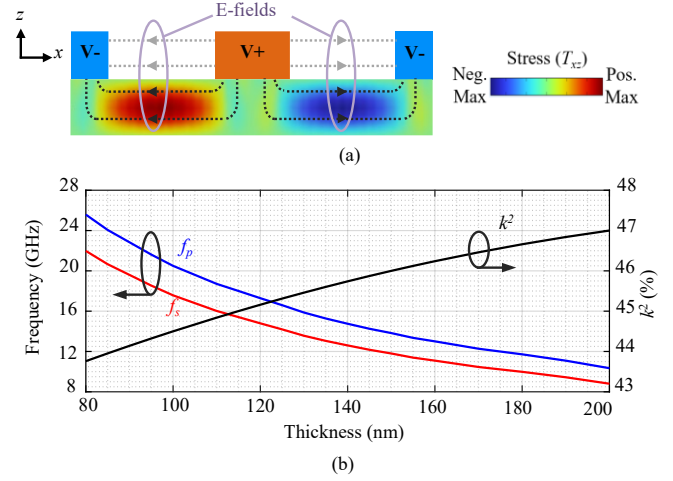
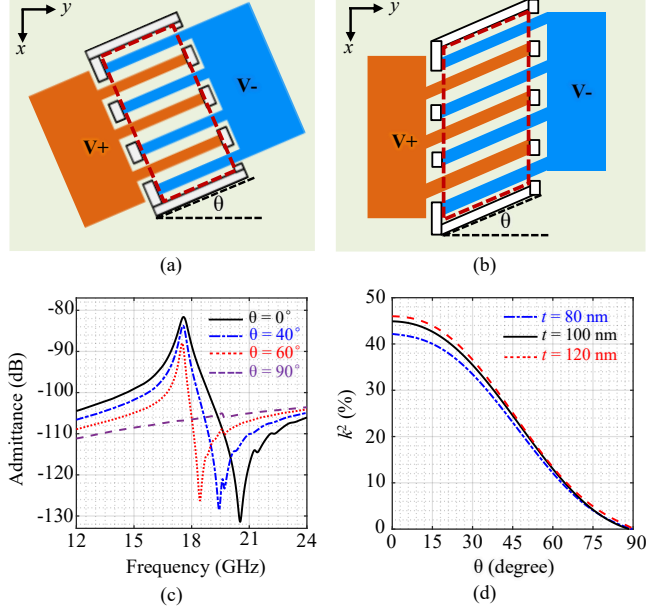


Fig. 3. (a) Simulated stress ( $T_{xz}$ ) mode shape of at the A1 resonance with illustrative lateral-excited E-fields (dimensions are not to scale). (b) Dispersion curves of the A1 resonance at different film thicknesses along with the perceived  $k^2$ .

smaller than the lateral acoustic wavelength [46]. In 128° Y-cut TFLN, the piezoelectric constant  $e_{15}$  is dominant [47], resulting in the strong excitation of the A1 mode characterized by shear stress ( $T_{xz}$ ). To illustrate the thickness dependence of A1 resonances, we performed a parametric study of a unit cell with two pairs of IDEs subjected to alternate voltage inputs in COMSOL FEA. Periodic boundary conditions were assigned to four lateral edges of the unit cell, while its top and bottom were sandwiched by air layers. The simulated A1 mode pattern, showing  $T_{xz}$  distribution, is presented in Fig. 3(a). The resulting dispersion curves for  $f_s$  and  $f_p$ , along with the perceived  $k^2$  calculated by (1), are plotted in Fig. 3(b). As the TFLN thickness increases, both  $f_s$  and  $f_p$  decrease, indicating that the center frequency  $f_c$  of the filter can be tuned by adjusting the TFLN thickness. In addition to the capability to scale the operating frequency, our study also reveals that static capacitance  $C_0$  is proportional to the TFLN thickness. As a result, the resonator impedance,  $Z_{res} \propto 1/(f_c C_0)$ , remains constant with variations in thickness. This notable property will be further discussed in Section IV.

#### B. In-plane Anisotropic Properties of 128° Y-cut TFLN

The anisotropic piezoelectric constants of TFLN can be evaluated by transforming the original material property matrices of the unrotated crystal [48] using the Euler angle rotations. These angles define the orientation of the device coordinate system relative to the material coordinate system, following the  $z$ - $x$ - $z$  rotation convention [49]. For 128° Y-cut TFLN, the corresponding Euler angles are  $(0^\circ, -38^\circ, 0^\circ)$  [35]. The corresponding material axes ( $X$ ,  $Y$ ,  $Z$ ), referenced to the local wafer axes ( $x$ ,  $y$ ,  $z$ ), are illustrated in Fig. 2(a). Due to a change in the lateral E-field orientation with respect to the crystal axes, an in-plane rotation of the IDEs on the 128° Y-cut TFLN platform results in a reduction of the effective piezoelectric constant  $e_{15}$ . This reorientation can be achieved either by rotating the entire resonator or by tilting only the IDEs within the active region, as illustrated in Figs. 4(a) and 4(b), respectively.



**Fig. 4.** Lateral E-field reorientation by (a) rotating the entire resonator and (b) tilting IDEs within the active region. (c) Simulated resonator admittance at different  $\theta$  with a thickness of 100 nm, indicating the orientation dependency of  $k^2$ . (d)  $k^2$  vs.  $\theta$  at several TFLN thicknesses ( $t$ ).

Although the dependency of  $e_{15}$  on the rotation has been reported in [50], it must be pointed out that there is no closed-form equation describing the relation between  $k^2$  and the orientation angle  $\theta$ , and the determination of  $k^2$  is heavily reliant on empirical study. The results from our unit cell FEA orientation study, plotted in Fig. 4(c), reveal that  $f_s$  barely changes with the thickness. On the contrary,  $f_p$  exhibits a strong dependency on  $\theta$ . The perceived  $k^2$  variations at different  $\theta$  and thicknesses obtained from parametric studies are shown in Fig. 4(d). Such in-plane rotation behavior of  $k^2$  introduces an additional design knob for filter design that allows for multiple filters with arbitrary FBWs on the same wafer.

#### IV. FILTER DESIGN AND SIMULATIONS

##### A. Three-Element Filter Design

Following the principle outlined in Section II, the FBW of a three-element filter can be customized through in-plane rotation of IDEs in  $128^\circ$  Y-cut TFLN. For example, an FBW-tuned filter shown in Fig. 5(a) can be realized by adjusting  $k^2$  of each resonator, as illustrated in Fig. 5(b). It is important to note that  $f_s$  and  $f_p$  of series and shunt resonators, respectively, are aligned to minimize IL. Since  $f_s$  barely changes with IDE orientation, the series resonator can be rotated to the required angle while maintaining a fixed active region thickness. In contrast, both the thickness and orientation of the shunt resonator must be carefully determined. Once the passband of the filter is defined,  $C_0$  of each resonator can be tailored to achieve both impedance matching (e.g.,  $50 \Omega$ ) and the desired transmission characteristics. Notably, using a larger shunt resonator (i.e., larger  $C_0$ ) improves OoB rejection but increases IL.

In addition to FBW control, in-plane orientation enables tuning of TZs to different frequencies. For instance, the shunt resonators in the three-element filter can be designed with

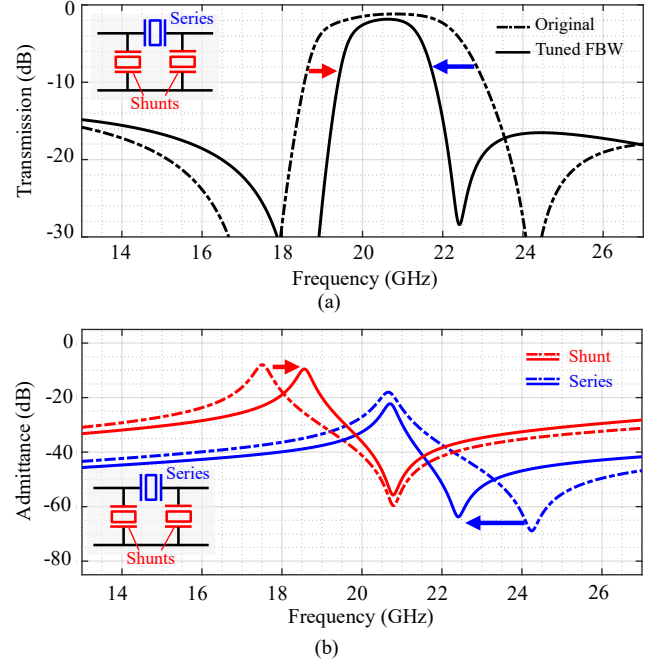


**Fig. 5.** (a) FBW of the three-element filter is controlled by rotating the IDEs of each resonator. (b)  $k^2$  tuning in each resonator.

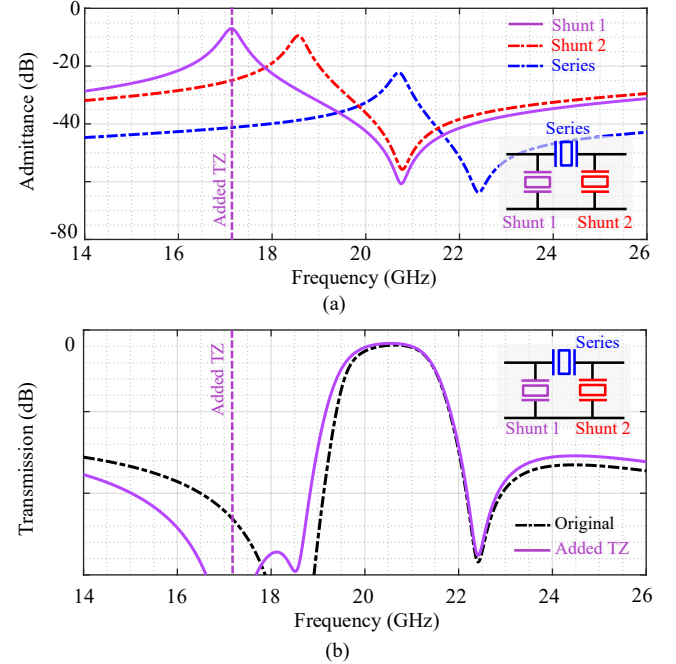


**Fig. 6.** (a) An additional TZ is introduced by changing the properties of one shunt resonator. (b) OoB rejection can be improved by the added TZ.

different  $f_s$  and  $k^2$  to introduce an additional TZ, as shown in Fig. 6(a). The added TZ can be strategically positioned to enhance either the selectivity by sharpening the passband roll-off or improve the OoB rejection (defined as a minimum IL within 10BW away from  $f_c$ ) at the lower band, as illustrated in Fig. 6(b). Notably, in the latter case, the passband of the filter becomes slightly higher as the shunt resonator contributing to the close-in rejection is smaller and the added TZ ‘stretches’ the filter response.



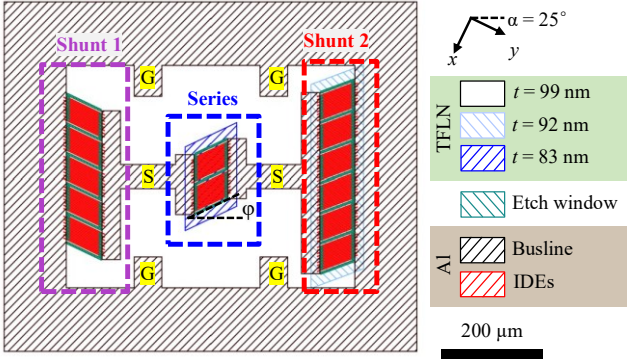


Fig. 7. Three-element filter layout.

TABLE I Design Parameters of Three-Element Prototype

Component	mBVD parameters	Device realization
Series	$f_s = 21$ GHz	$t = 83$ nm (2 trims)
	$k^2 = 17\%$	$\theta = 50^\circ$ ( $\varphi = 25^\circ$ )
	$C_0 = 48$ fF	$N_g = 16$
		$N_g = 2$
		$l_e = 62$ $\mu$ m
Shunt 1	$f_s = 17.9$ GHz	$t = 99$ nm (no trim)
	$k^2 = 42.5\%$	$\theta = 0^\circ$ ( $\varphi = -25^\circ$ )
	$C_0 = 168$ fF	$N_g = 16$
		$N_g = 5$
		$l_e = 68$ $\mu$ m
Shunt 2	$f_s = 19.1$ GHz	$t = 92$ nm (1 trim)
	$k^2 = 22.6\%$	$\theta = 45^\circ$ ( $\varphi = 20^\circ$ )
	$C_0 = 169$ fF	$N_g = 17$
		$N_g = 6$
		$l_e = 63$ $\mu$ m

$$w_e = 2.2 \mu\text{m}, w_g = 0.8 \mu\text{m}, \text{ and } A = 6 \mu\text{m}.$$

To demonstrate the proposed design approach, a 50- $\Omega$  BPF centered at 20.5 GHz was designed using one series resonator and two distinct shunt resonators. In our previous study [1], we presented a straightforward method of tuning frequency by rotating the entire resonators. In this work, we extend that concept by combining resonator rotation with IDE tilting to further reduce the overall filter footprint. The targeted FBW of 9.5% was achieved by simultaneously tuning the in-plane orientation, using a global filter rotation angle of  $\alpha = 25^\circ$  and an additional IDE tilting angle  $\varphi = \theta - \alpha$ , as illustrated in Fig. 7, and adjusting the TFLN thickness of each resonator. Note that the axes  $x$  and  $y$  here indicate the local coordinate of the wafer, not the material. The required  $C_0$  for each resonator was realized by calculating the appropriate number of IDE pairs and their finger lengths  $l_e$ , using the capacitance density obtained from the unit cell simulation. For fabrication purposes, the total number of IDEs was evenly divided into several groups, defined by the number of groups ( $N_g$ ) and the number of IDEs per group ( $N_e$ ), to ensure complete release of the active region while minimizing the risk of structural collapse. The design parameters were optimized to achieve a well-balanced trade-off

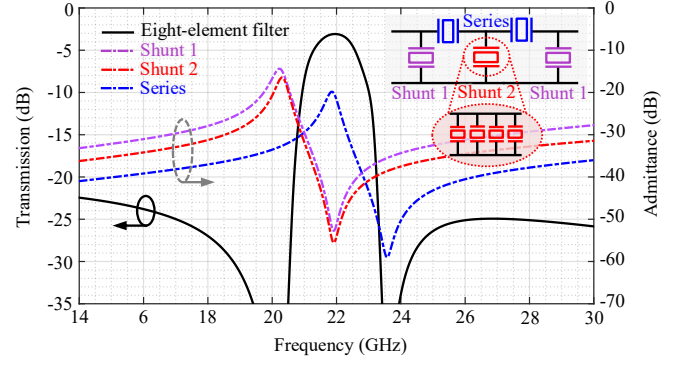


Fig. 8. Frequency responses of the eight-element filter, with an equivalent circuit schematic shown in the inset, and its constituent resonators.

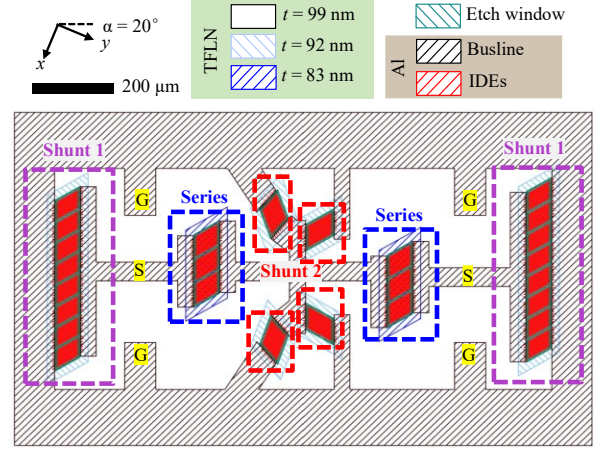


Fig. 9. Eight-element filter layout.

between IL and OoB rejection. Table I summarizes the optimized design parameters for the proposed filter prototype. Note that the target  $f_s$  of each resonator was realized through a series of TFLN thickness trimming steps. The detailed fabrication process will be explained in Section V. It is important to note that  $Q$ ,  $R_s$ , and  $L_s$  of each resonator used in our design are estimated based on our previous studies [37]–[39], [42].

### B. Eight-Element Filter Design

To further demonstrate the functionality of the proposed design approach, a higher-order filter was developed. Film thickness inspection revealed a slight thickness variation in our TFLN wafer, with the film being approximately 3 nm thinner at the intended fabrication location. To avoid additional fabrication steps, the eight-element filter was designed to reuse the same trimming depths as those used in the three-element prototype (7 nm and 9 nm for the first and second trims, respectively). As a result, the center frequency  $f_c$  of the eight-element prototype is 22.0 GHz. Moreover, the orientation combination was slightly adjusted to achieve an FBW of 6.4% in this case to illustrate the capability of fabricating filters with different FBWs on the same wafer by using the proposed methodology.

To mitigate the increased IL associated with additional series resonators, the design employs two identical series resonators and a single Shunt 2 resonator positioned between them, with two identical Shunt 1 resonators at the input ports. The

TABLE II Design Parameters of Eight-Element Prototype

Component	mBVD parameters	Device realization
Series	$f_s = 22.13$ GHz	$t = 80$ nm (2 trims)
	$k^2 = 16.5\%$	$\theta = 50^\circ$
	$C_0 = 77$ fF	$N_e = 16$
		$N_g = 3$
		$l_e = 63$ $\mu\text{m}$
	$Q = 80, R_s = 3.5$ $\Omega, L_s = 0.1$ nH	
Shunt 1	$f_s = 20.5$ GHz	$t = 89$ nm (1 trim)
	$k^2 = 17.5\%$	$\theta = 50^\circ$
	$C_0 = 180$ fF	$N_e = 16$
		$N_g = 8$
		$l_e = 61$ $\mu\text{m}$
	$Q = 80, R_s = 2.5$ $\Omega, L_s = 0.05$ nH	
Shunt 2	$f_s = 20.5$ GHz	$t = 89$ nm (1 trim)
	$k^2 = 17.5\%$	$\theta = 50^\circ$
	$C_0 = 130$ fF	$N_e = 17$
		$N_g = 4^*$
		$l_e = 69$ $\mu\text{m}$
	$Q = 80, R_s = 2.5$ $\Omega, L_s = 0.05$ nH	

$w_e = 2.2$   $\mu\text{m}$ ,  $w_g = 0.8$   $\mu\text{m}$ , and  $l = 6$   $\mu\text{m}$ .

\*Shunt 2 is divided into 4 identical resonators ( $C_0 = 32.5$  fF each).

simulated transmission response of this filter is shown in Fig. 8, alongside that of the lower-order prototype, highlighting a significant improvement in OoB rejection. To accommodate layout wiring and spacing constraints, the Shunt 2 resonator was subdivided into four smaller, identical resonators, as depicted in Fig. 9. The design parameters for the eight-element prototype are summarized in Table II.

### C. Impact of Constant Resonator Impedance

As mentioned earlier in Section III, the resonator impedance  $Z_{res} \propto 1/(f_c C_0)$  remains constant despite variations in film thickness. This elegant property enables proportional scaling of the operating frequency band by simply adjusting the base thickness, as illustrated in Fig. 10, while preserving the same filter layout. Although this characteristic lies outside the primary scope of this study, it is worth noting that such behavior is unique to XBAR filters and is not observed in incumbent FBAR and SAW technologies [1]. This distinctive capability opens new avenues for further exploration in acoustic filter design.

## V. FABRICATION RESULTS AND DISCUSSIONS

### A. Device Fabrication

Fig. 11 summarizes the fabrication process utilized in this work. The process begins with a TFLN-on-aSi-on-Sapphire wafer provided by NGK Insulator Ltd. For this demonstration, target thicknesses were realized through two sequential ion milling steps with distinct exposure times: the first trim, removing 7 nm, was applied to both shunt and series resonators; the second trim, removing an additional 9 nm, was applied exclusively to the series resonators. In each step, high-energy ions (e.g., ionized Ar gas) bombard the surface within a vacuum chamber, selectively thinning the TFLN layer and thereby

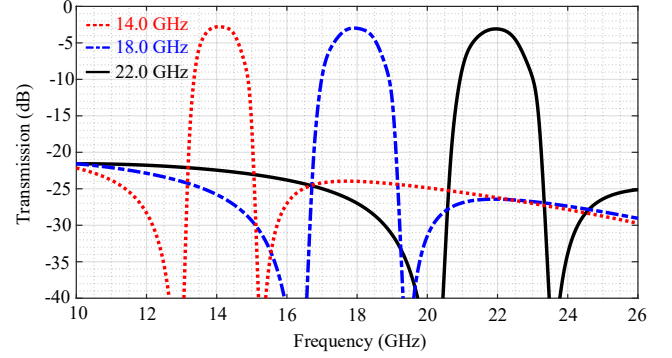


Fig. 10. Simulated frequency-scaled filters with the same layout.

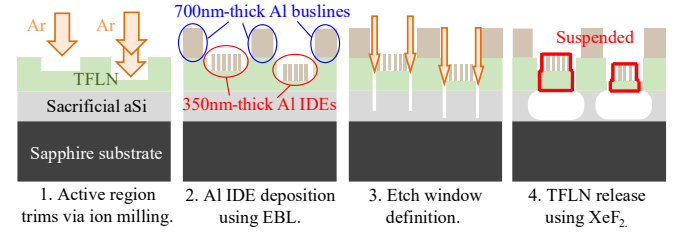


Fig. 11. Fabrication process.

defining the active region thickness of each resonator. Notably, this physical etching process preserves the crystalline quality of the TFLN layer, which is essential for retaining its piezoelectric properties [51]. Due to the minor thickness variations across the wafer for research prototyping purposes, frequency shifts in the devices are expected. However, as discussed in Section IV, such variations primarily result in a uniform shift of the center frequency  $f_c$ , provided that the trimmed regions undergo consistent thinning.

Following the thinning step, aluminum metallization is patterned on the trimmed wafer using electron beam lithography (EBL). The metallization consists of 350 nm-thick IDEs and 700 nm-thick buslines. After the Al deposition, etch windows are defined by ion milling. These windows serve to confine the active regions and enable thin-film suspension. The release process is performed using xenon difluoride ( $\text{XeF}_2$ ), which selectively removes the sacrificial amorphous silicon (aSi) layer beneath the TFLN. This step must be executed with care, as the delicate, small-featured IDEs are the sole structural support for the suspended resonators and are susceptible to collapse if over-etched or poorly supported.

In this work, we fabricated and characterized three groups of test structures to validate the proposed design methodology: individual resonator behavior, and two prototype filter designs. First, to verify the concept of resonator rotation, a series of XBARS with varying in-plane rotation angles and film thicknesses were fabricated. For the prototype filters, their constituent resonators were also fabricated separately alongside the filter structures to enable direct monitoring of their individual resonance responses.

### B. Resonator Measurement

Three sets of XBARS, each with a different TFLN thickness, were fabricated and measured. Each set included eight devices with IDE tilting angles ranging from  $0^\circ$  to  $70^\circ$ , as shown in Fig. 12. The series resonance frequency  $f_s$  was extracted from

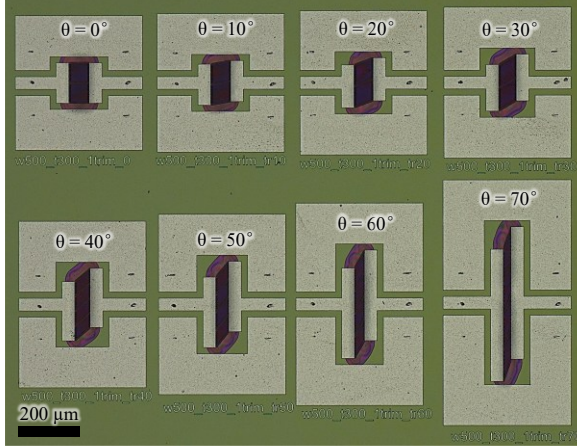


**Fig. 12.** A group of resonators with varying IDE angles, but identical number of trims.

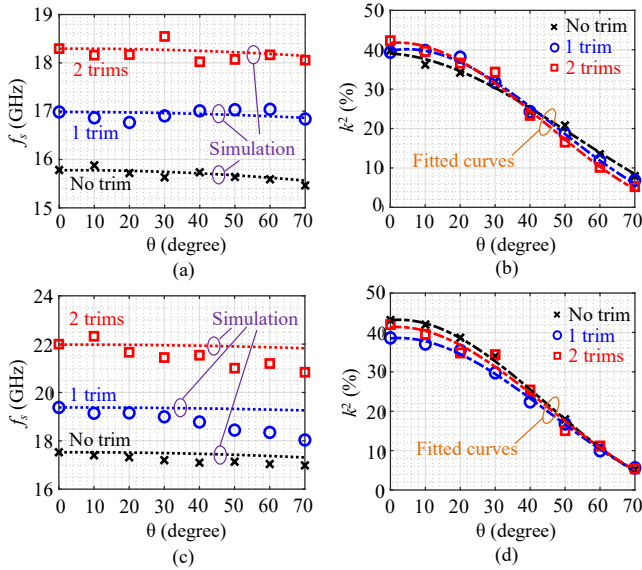


**Fig. 13.** Extracted resonator parameters from two study sets. Set 1: (a)  $f_s$  vs.  $\theta$  with simulation-based predictions (dotted lines), and (b)  $k^2$  vs.  $\theta$  with fitted curves (dashed lines). Set 2: (c)  $f_s$  vs.  $\theta$  and (d)  $k^2$  vs.  $\theta$ , following the same notation.

the measured two-port  $S$ -parameters, using a Keysight E8361C PNA vector network analyzer (VNA) with GSG probes, via standard  $Y_{21}$  conversion [9]. As shown in Fig. 13(a), three distinct  $f_s$  ranges are observed, corresponding to the three TFLN thicknesses. By comparing the measurements with the predicted trend from the simulations, extrapolated from  $f_s$  at  $\theta = 0^\circ$ , the effects of local thickness variation are evident. Fig. 13(b) presents the extracted  $k^2$ , along with their fitted curves. The observed trends are closely matched with the simulations presented in Fig. 4, with minor discrepancies caused by spurious modes, as well as parasitic inductance due to EM resonance, as shown in Fig. 14. These effects introduce inaccuracies when directly applying (1) to determine  $k^2$  from the measured  $f_s$  and  $f_p$ . To accurately extract  $k^2$  of the devices, modeling based on the mBVD circuit must be performed. For further discussion on precise modeling and treatment of piezoelectric devices under EM interaction, readers are referred to [52].

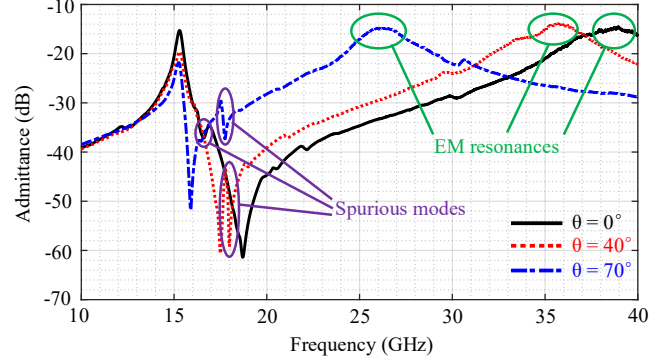


**Fig. 14.** Measurement samples from the untrimmed group of the study Set 1, indicating spurious modes and EM resonance.

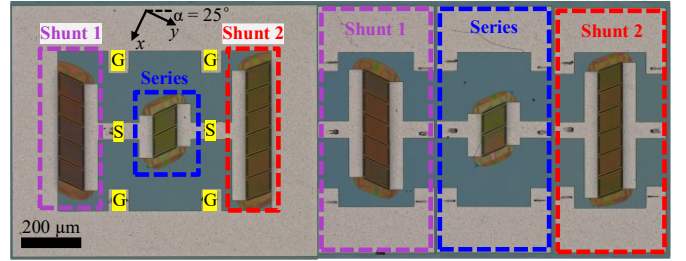


**Fig. 15.** The fabricated three-element filter prototype and its standalone constituent resonators.

To evaluate the impact of initial film thickness variation across the wafer, an identical set of devices was fabricated at a different location on the same sample. Following Fig. 13(c), the obtained  $f_s$  values differ significantly from those in Set 1, underscoring the critical importance of thickness uniformity for consistent device performance. Nevertheless, the trend of  $k^2$  variation with respect to IDE tilting angle remains consistent, as depicted in Fig. 13(d).

### C. Three-Element Filter Prototype

Fig. 15 shows the in-house fabricated three-element filter prototype alongside its standalone resonators. The measured  $S_{21}$  obtained using the VNA is plotted in Fig. 16(a), together with the simulated response from the simulation-based design and the fitted post-processed mBVD network. We will use the fitted model to further analyze our design. A magnified view of the passband, shown in Fig. 16(b), demonstrates close agreement between measurement and simulation. Regarding impedance matching, Figs. 16(c) and (d) indicate that the filter is well-matched to a  $50\Omega$  reference at both ports. The observed asymmetry is due to the use of different shunt resonators, which introduce different input impedances at each port.

Table III summarizes key filter metrics obtained from the simulation-based design, measurement, and the fitted model for the three-element filter prototype. Note that the OoB rejection in this work is defined by a minimum IL within the frequency range  $f_c \pm 10\text{BW}$  from the passband. The fabricated device exhibits a slightly higher insertion loss of 1.79 dB and a reduced FBW of 8.58%, compared to the designed 9.54%. The measured admittance responses of standalone resonators fabricated adjacent to the filter are compared with the design values, as shown in Fig. 17, to examine the discrepancies.



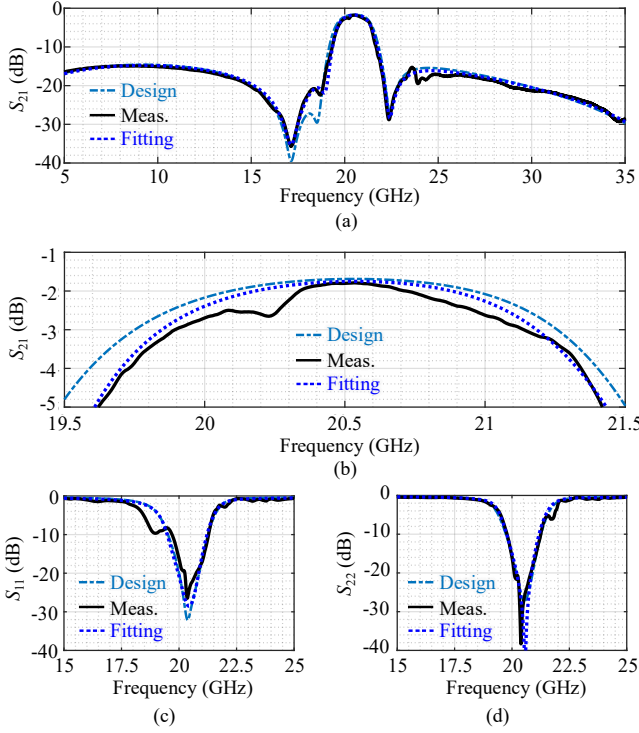


**Fig. 16.** Measurement results compared to the simulation-based design and mBVD post-measurement fitting of the three-element prototype: (a)  $S_{21}$ , (b) a magnified passband, (c)  $S_{11}$ , and (d)  $S_{22}$ .

**TABLE III** Simulation and Measurement Comparisons for Three-Element Filter Characteristics

Parameters	Simulation	Measurement	Fitted model
$f_c$	20.5 GHz	20.5 GHz	20.5 GHz
Min. IL	1.69 dB	1.79 dB	1.79 dB
3dB-FBW	9.54%	8.58%	8.78%
20dB-FBW	16.8%	16.5%	15.9%
Lower OoB Rej.	14.59 dB @9.2 GHz	14.92 dB @8.6 GHz	14.78 dB @9.7 GHz
Upper OoB Rej.	15.42 dB @24.5 GHz	15.24 dB @23.6 GHz	16.36 dB @24.8 GHz

According to Table IV, the fitted mBVD model parameters extracted from the fabricated filter closely align with the design values, indicating only minor deviations and contributing to the overall accurate response. It can be inferred that a primary source of deviation is the slightly overestimated  $k^2$  in the simulation, which significantly impacts the FBW. In addition, layout-induced parasitics,  $R_s$  and  $L_s$ , are other contributing factors. Furthermore, spurious modes present in the fabricated prototype potentially contribute to the passband ripples we observed in the filter measurements.

#### D. Eight-Element Filter Prototype

The images of the fabricated eight-element filter prototype and its standalone resonators are given in Fig. 18. Compared to the three-element design, this prototype poses greater challenges for modeling with a simple mBVD circuit network, due to increased complexity from multiple resonator variations, a larger layout, and stronger spurious mode effects. To reduce complexity in fitting the filter response, we assume that the two Shunt 1 resonators are identical, as are the four Shunt 2

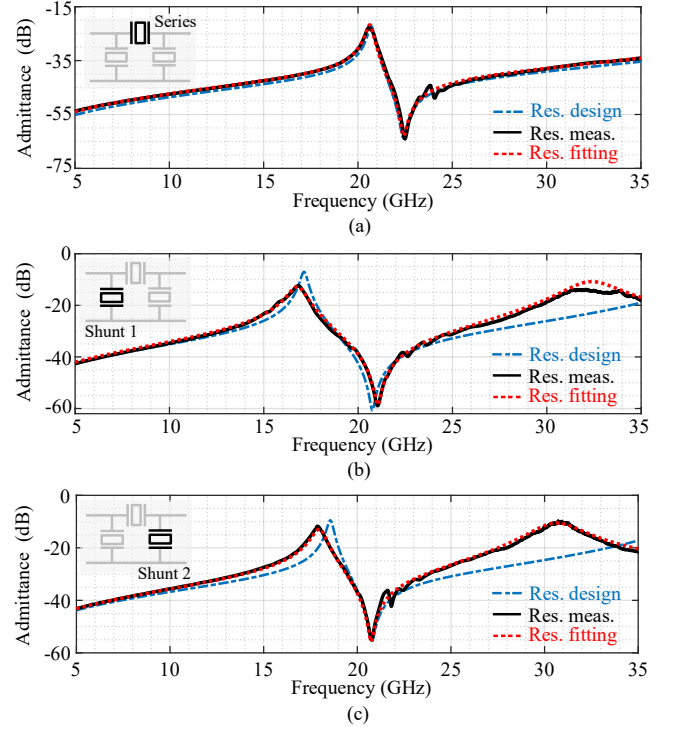


**Fig. 17.** Admittance comparisons of the design, individual resonator measurement, and resonator fitting of the three-element prototype: (a) Series, (b) Shunt 1, and (c) Shunt 2, respectively.

**TABLE IV** mBVD Model Parameter Comparisons of Three-Element Filter

Resonator		$f_r$ (GHz)	$k^2$ (%)	$Q$	$C_0$ (fF)	$R_s$ ( $\Omega$ )	$L_s$ (nH)
Series	Design	21.00	17.0	80	48	3	0.2
	Filter fitting	20.99	17.1	76	47	1.5	0.28
	Res. fitting	20.95	17.9	80	55	6	0.18
Shunt 1	Design	17.90	42.5	80	168	1	0.1
	Filter fitting	18.05	41.5	76	177	1.5	0.11
	Res. fitting	18.25	40.7	70	178	3.9	0.16
Shunt 2	Design	19.10	22.6	80	169	1	0.1
	Filter fitting	19.30	19.5	70	175	1.5	0.08
	Res. fitting	19.10	22.1	86	179	3.6	0.17

resonators, in line with the original design intent. Despite this simplification, the comparisons in Table V and the close-up view in Fig. 19(b) confirm that the proposed modeling approach is sufficiently accurate for passband characterization. Notably, the asymmetry in the S-parameters, as shown in Figs. 19(c) and (d), can be attributed to several factors, including mismatches between resonators that were designed to be identical and the influence of parasitic EM effects.

To further investigate the discrepancies, the standalone resonator measurements and their corresponding mBVD model fittings are compared with the design parameters, as shown in Figs. 20(a)–(c). Following the data summarized in Table V, the design and measured parameters, both from filter fitting and standalone resonator fitting, are generally well-aligned, with minor discrepancies in  $f_s$  and  $k^2$  due to thickness variations and simulation accuracy. It is important to note that  $R_s$  and  $L_s$  are inherently layout-dependent and are expected to differ across the three cases. These results suggest that the main contributors to the observed deviations are likely mismatches between



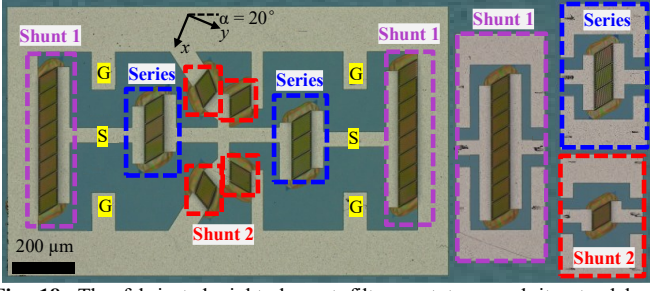


Fig. 18. The fabricated eight-element filter prototype and its standalone constituent resonators.

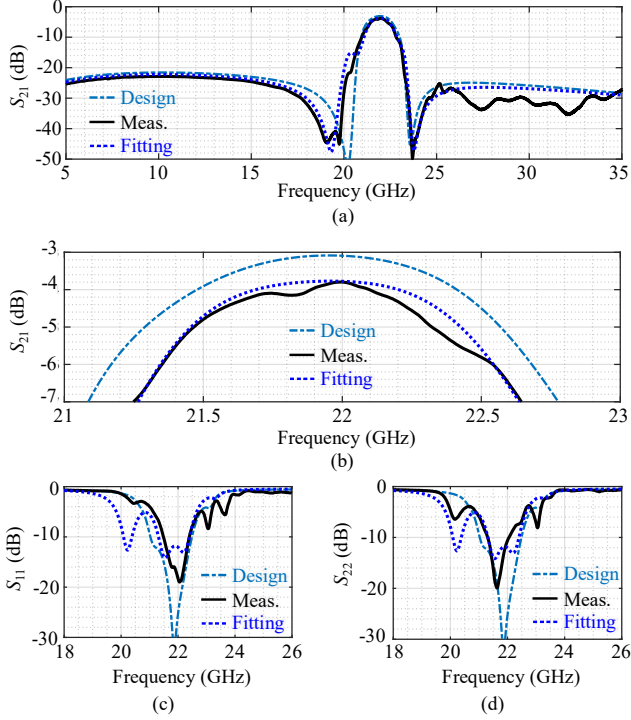


Fig. 19. Measurement results compared to the simulation-based design and mBVD post-measurement fitting of the eight-element prototype: (a)  $S_{21}$ , (b) a magnified passband, (c)  $S_{11}$ , and (d)  $S_{22}$ .

TABLE V Simulation and Measurement Comparisons for Eight-Element Filter Characteristics

Parameters	Simulation	Measurement	Fitted model
$f_c$	22.0 GHz	22.0 GHz	22.0 GHz
Min. IL	3.08 dB	3.80 dB	3.80 dB
3dB-FBW	6.40%	6.12%	6.12%
20dB-FBW	12.1%	14.5%	18.8%
Lower OoB Rej.	21.57 dB @10.4 GHz	22.97 dB @11.5 GHz	22.24 dB @10.2 GHz
Upper OoB Rej.	25.94 dB @26.8 GHz	25.30 dB @25.2 GHz	26.45 dB @27.8 GHz

nominally identical resonators, as well as the influence of EM effects.

#### E. Discussions and Comparison to the State of the Art

Our prototype fabrication and measurements have highlighted two important intertwined factors essential for designing acoustic BPF with precise control over the FBW and center frequency  $f_c$ : modeling accuracy and process variations. While  $f_c$  can be estimated from  $f_s$  of the series resonator, which is

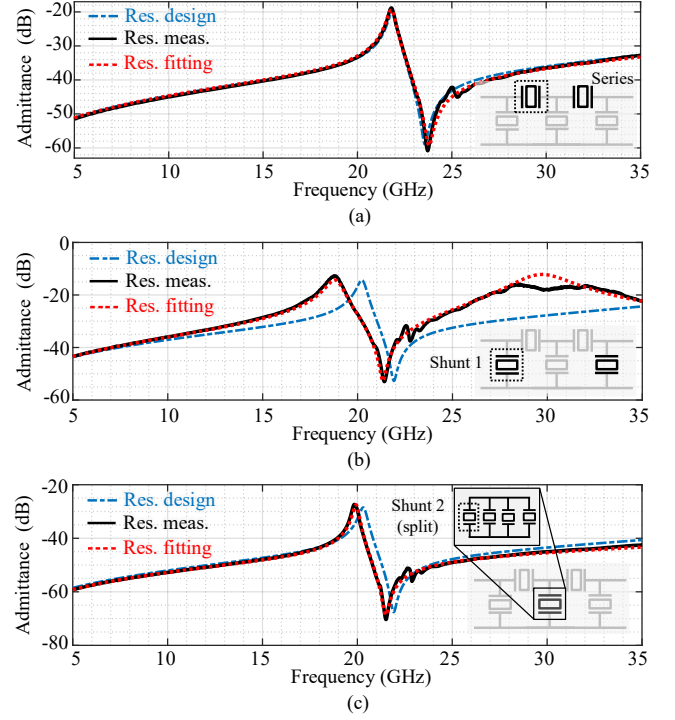


Fig. 20. Admittance comparisons of the design, individual resonator measurement, and resonator fitting of the eight-element prototype: (a) Series, (b) Shunt 1, and (c) Shunt 2 (split), respectively.

TABLE VI mBVD Model Parameter Comparisons of Eight-Element Filter

Resonator		$f_s$ (GHz)	$k^2$ (%)	$Q$	$C_0$ (fF)	$R_s$ ( $\Omega$ )	$L_s$ (nH)
Series	Design	22.13	16.5	80	77	3.5	0.1
	Filter fitting	22.10	19.5	70	71	3.2	0.07
	Res. fitting	22.10	17.5	70	75	3	0.10
Shunt 1	Design	20.50	18.0	80	180	2.5	0.05
	Filter fitting	19.49	18.8	60	182	2.0	0.04
	Res. fitting	20.00	17.0	80	180	4	0.18
Shunt 2 <sup>a</sup>	Design	20.50	17.5	80	32.5	2.5	0.05
	Filter fitting	20.83	19.0	70	31	5.0	0.04
	Res. Fitting	20.00	19.0	76	30	2.8	0.08

<sup>a</sup>Split resonator.

largely determined by the precision of active region etching and the thickness uniformity of the TFLN platform, it is evident that accurate prediction of  $k^2$  is most crucial. The value of  $k^2$  strongly influences overall filter performance, as it governs the location of TZs and, consequently, underpins the required etching depths of all active regions from the initial wafer thickness.

The findings show that even small variations in resonance frequencies can result in noticeable discrepancies, especially in the higher-order BPF containing multiple resonators. Although the mBVD circuit model offers sufficiently accurate predictions, the ability to account for electromagnetic (EM) resonances induced by the filter layout is indispensable. In fact, such EM behavior could be strategically exploited to increase design flexibility through EM-acoustic co-design. This way we can potentially enhance filter characteristics, such as FBW improvement by increasing the separation between  $f_s$  and  $f_p$ , and independently strengthen OoB rejection through the

TABLE VII  
REPORTED FR3 ACOUSTIC FILTERS BEYOND 10 GHz

Ref.	Technology	$f_c$ (GHz)	IL (dB)	Rej. (dB)*	FBW (%)	Monolithic $f_c$ and FBW
[38]	TFLN XBAR	23.5	2.4	13.6	18.2	No
[39]	TFLN XBAR	22.1	1.6	11.9	19.8	No
[40]	TFLN XBAR with inductors	19.0	8.0	13.0	2.4	No
[41]	Bi-layer P3F AlScN FBAR	10.7	0.7	N/A	5.3	No
[42]	Bi-layer P3F TFLN XBAR	23.8	1.5	9.5	19.4	No
[43]	4-layer P3F AlScN FBAR	17.4	1.9	5.1	3.9	No
		17.4	3.3	12.8	3.4	No
<b>This work</b>	<b>TFLN XBAR</b>	<b>20.5</b>	<b>1.79</b>	<b>14.92</b>	<b>8.58</b>	<b>Yes</b>
		<b>22.0</b>	<b>3.80</b>	<b>22.97</b>	<b>6.12</b>	<b>Yes</b>

\*OoB rejection is defined as the minimum IL within the frequency range  $f_c \pm 10\text{BW}$  from the passband; N/A: insufficient data.

introduction or repositioning of additional TZs. We aim to explore this approach in our future work.

As shown in Table VII, our design approach has demonstrated significant advancements in acoustic filter design for FR3 operation in terms of both performance and design degrees of freedom. Our three-element prototype achieves low IL while retaining relatively high OoB rejection. Although the eight-element prototype incurs approximately 2 dB higher IL and exhibits impairments due to fabrication challenges, it provides an OoB rejection improvement of over 8 dB compared to its lower-order counterpart. More importantly, our innovation enables monolithic control over BPF characteristics, allowing for the implementation of multiple filters on a single wafer. With further refinement in device modeling and process accuracy, this approach could pave the way for high-performance, chip-scale monolithic multiplexers and filter banks.

Compared to other advanced filter technologies, as indicated in Table VIII, our work highlights competitive overall performance, with a great balance between IL, FBW design, OoB rejection, and selectivity within an extremely compact planar footprint. A strong chip-scale competitor of acoustic technology at FR3 and beyond is IPD [8], which offers superior OoB rejection and significantly lower IL. However, the acoustic platform's ability to achieve sharp roll-off characteristics, enabled by high-Q resonances, provides distinct advantages for mobile applications operating in increasingly crowded spectral environments. The authors believe that the hybrid integration of acoustic and IPD technologies will be a promising path forward to realize high-performance, scalable RF front-end solutions for future wireless systems.

## VI. CONCLUSION

This paper comprehensively introduces a new systematic approach for monolithic design of acoustic filters at FR-3. A key innovation lies in correlating bandpass filter (BPF) characteristics with the antiresonance behavior of XBARs, effectively modeled using a simple mBVD circuit model. The proposed circuit-based method leverages the in-plane

TABLE VIII  
Advanced Filter Technology COMPARISONS

Ref.	Technology	$f_c$ (GHz)	Area ( $\mu\text{m}^2$ )	Height (mm)	IL (dB)	Rej. (dB)*	FBW (%)	20-dB FBW (%)
[8]	GaAs-IPD	28	0.003 <sup>†</sup>	N/A	0.76	18.6	22	49.6
[12]	DSG-PCB	4.94	0.12	0.5	1.8	25.8	64	114
[14]	SIW-PCB	10.05	0.24	0.5	0.82	45	12.2	17.4
[15]	SIW-TSV	17.96	0.03	0.2	0.85	N/A	89.2	136
[16]	SIW-TGV	32	0.18	0.4	0.96	N/A	13.1	28.2
[19]	SIW-LTCC	27	0.001 <sup>†</sup>	2.8 <sup>††</sup>	1.36	22.0	18.2	61.5
<b>This work</b>	<b>TFLN XBAR (MEMS)</b>	<b>20.5</b>	<b>0.003</b>	<b>0.5</b>	<b>1.79</b>	<b>14.92</b>	<b>8.58<sup>#</sup></b>	<b>16.5</b>
		<b>22.0</b>	<b>0.007</b>	<b>0.5</b>	<b>3.80</b>	<b>22.97</b>	<b>6.12<sup>#</sup></b>	<b>14.5</b>

\*OoB rejection is defined as the minimum IL within the frequency range  $f_c \pm 10\text{BW}$  from the passband; <sup>†</sup> excluded GSG probes; <sup>††</sup> estimated from the reported layer thickness; <sup>#</sup> customized FBW; N/A: insufficient data.

anisotropic piezoelectricity of Al XBARs in 128° Y-cut TFLN, enabling flexible filter customization solely through planar orientation control. The design demonstration—from multiphysics device simulation to fabrication—culminates in two BPF prototypes with tailored FBWs. A thorough analysis reveals key insights and challenges associated with modeling and fabrication. With further development, the proposed methodology would pave the way for chip-scale multiplexers and filter banks with precise band selection for next-generation wireless mobile communications.

## ACKNOWLEDGMENT

The authors thank Dr. Ben Griffin, Dr. Todd Bauer, and Dr. Zachary Fishman for helpful discussions.

## REFERENCES

- [1] O. Barrera *et al.*, "Frequency and bandwidth design toward millimeter-wave thin-film lithium niobate acoustic filters," *IEEE Microw. Wirel. Tech. Lett.*, doi: [10.1109/LMWT.2025.3559400](https://doi.org/10.1109/LMWT.2025.3559400).
- [2] C.-X. Wang *et al.*, "On the road to 6G: Visions, requirements, key technologies, and testbeds," *IEEE Commun. Surv. Tutor.*, vol. 25, no. 2, pp. 905–974, 2023, doi: [10.1109/COMST.2023.3249835](https://doi.org/10.1109/COMST.2023.3249835).
- [3] J. G. Andrews, T. E. Humphreys, and T. Ji, "6G takes shape," *IEEE BITS*, vol. 4, no. 1, pp. 2–24, March 2024, doi: [10.1109/MBITS.2024.3504521](https://doi.org/10.1109/MBITS.2024.3504521).
- [4] H. Miao *et al.*, "Sub-6 GHz to mmWave for 5G-Advanced and beyond: Channel measurements, characteristics and impact on system performance," *IEEE J. Sel. Areas Commun.*, vol. 41, no. 6, pp. 1945–1960, June 2023, doi: [10.1109/JSAC.2023.3274175](https://doi.org/10.1109/JSAC.2023.3274175).
- [5] S. Kang *et al.*, "Cellular wireless networks in the upper mid-band," *IEEE Open J. Commun. Soc.*, vol. 5, pp. 2058–2075, 2024, doi: [10.1109/OJCOMS.2024.3373368](https://doi.org/10.1109/OJCOMS.2024.3373368).
- [6] D. Shakya *et al.*, "Comprehensive FR1(C) and FR3 lower and upper mid-band propagation and material penetration loss measurements and channel models in indoor environment for 5G and 6G," *IEEE Open J. Commun. Soc.*, vol. 5, pp. 5192–5218, 2024, doi: [10.1109/OJCOMS.2024.3431686](https://doi.org/10.1109/OJCOMS.2024.3431686).
- [7] A. Davidson, *National Spectrum Strategy Implementation Plan*, Washington, DC, USA, Mar. 2024.
- [8] G. Shen, Z. He, W. Feng, B. Wen, Q. Xue, and W. Che, "Lumped-distributed on-chip resonators with multistubs reused and its application to stopband extended IPD bandpass filters," *IEEE Trans. Microw. Theory Tech.*, vol. 72, no. 4, pp. 2498–2507, April 2024, doi: [10.1109/TMTT.2023.3316358](https://doi.org/10.1109/TMTT.2023.3316358).
- [9] D. M. Pozar, *Microwave engineering*. Hoboken, NJ: Wiley, 2012.

- [10] J.-S. Hong, *Microstrip filters for RF/microwave applications*. Hoboken, N.J.: Wiley, 2011.
- [11] S. Xu, K. Ma, F. Meng, and K. S. Yeo, "Novel defected ground structure and two-side loading scheme for miniaturized dual-band SIW bandpass filter designs," *IEEE Microw. Wirel. Compon. Lett.*, vol. 25, no. 4, pp. 217-219, April 2015, doi: [10.1109/LMWC.2015.2400916](https://doi.org/10.1109/LMWC.2015.2400916).
- [12] W. Yuan, X. Liu, H. Lu, W. Wu and N. Yuan, "Flexible design method for microstrip bandstop, highpass, and bandpass filters using similar defected ground structures," *IEEE Access*, vol. 7, pp. 98453-98461, 2019, doi: [10.1109/ACCESS.2019.2928816](https://doi.org/10.1109/ACCESS.2019.2928816).
- [13] G. Lin and Y. Dong, "A compact, hybrid SIW filter with controllable transmission zeros and high selectivity," *IEEE Trans. Circuits Syst. II: Express Br.*, vol. 69, no. 4, pp. 2051-2055, April 2022, doi: [10.1109/TCSII.2022.3144268](https://doi.org/10.1109/TCSII.2022.3144268).
- [14] Y. Zhu, Y. Dong, J. Bornemann, L. Gu, and D. F. Mamedes, "SIW triplets including meander-line and CRLH resonators and their applications to quasi-elliptic filters," *IEEE Trans. Microw. Theory Tech.*, vol. 71, no. 5, pp. 2193-2206, May 2023, doi: [10.1109/TMTT.2022.3225447](https://doi.org/10.1109/TMTT.2022.3225447).
- [15] C. Fan, X. Liu, N. Liu, and Z. Zhu, "Compact bandpass filters with low loss and TZs based on 1/n mode circle-SIW in through silicon vias (TSVs) technology," *IEEE Trans. Microw. Theory Tech.*, vol. 72, no. 9, pp. 5095-5105, Sept. 2024, doi: [10.1109/TMTT.2024.3370823](https://doi.org/10.1109/TMTT.2024.3370823).
- [16] L. Wang *et al.*, "A low-loss slow wave SIW bandpass filter with blind vias using TGV technology," *IEEE Microw. Wirel. Tech. Lett.*, vol. 34, no. 3, pp. 271-274, March 2024, doi: [10.1109/LMWT.2024.3350110](https://doi.org/10.1109/LMWT.2024.3350110).
- [17] W. Li *et al.*, "Glass-based single-layer slow wave SIW filter with embedded composite right-/ left-handed resonator," *IEEE Trans. Microw. Theory Tech.*, vol. 73, no. 2, pp. 1105-1116, Feb. 2025, doi: [10.1109/TMTT.2024.3440250](https://doi.org/10.1109/TMTT.2024.3440250).
- [18] X. Huang, X. Zhang, L. Zhou, J. -X. Xu, and J. -F. Mao, "Low-loss self-packaged Ka-Band LTCC filter using artificial multimode SIW resonator," *IEEE Trans. Circuits Syst. II: Express Br.*, vol. 70, no. 2, pp. 451-455, Feb. 2023, doi: [10.1109/TCSII.2022.3173712](https://doi.org/10.1109/TCSII.2022.3173712).
- [19] G. Shen, W. Yang, W. Feng, Q. Xue, and W. Che, "Vertically stacked millimeter-wave LTCC filters with cavity-mode suppression for system-in-package application," *IEEE Trans. Microw. Theory Tech.*, vol. 71, no. 6, pp. 2532-2544, June 2023, doi: [10.1109/TMTT.2022.3226722](https://doi.org/10.1109/TMTT.2022.3226722).
- [20] D. Royer, D. P. Morgan, and E. Dieulesaint, *Elastic Waves in Solids I: Free and Guided Propagation*. Berlin, Germany: Springer, 2000.
- [21] S. Gong, R. Lu, Y. Yang, L. Gao, and A. E. Hassanien, "Microwave acoustic devices: Recent advances and outlook," *IEEE J. Microwaves*, vol. 1, no. 2, pp. 601-609, April 2021, doi: [10.1109/JMW.2021.3064825](https://doi.org/10.1109/JMW.2021.3064825).
- [22] A. Hagelauer *et al.*, "From microwave acoustic filters to millimeter-wave operation and new applications," *IEEE Journal of Microwaves*, vol. 3, no. 1, pp. 484-508, Jan. 2023, doi: [10.1109/JMW.2022.3226415](https://doi.org/10.1109/JMW.2022.3226415).
- [23] P. Warder and A. Link, "Golden age for filter design: Innovative and proven approaches for acoustic filter, duplexer, and multiplexer design," *IEEE Microw. Mag.*, vol. 16, no. 7, pp. 60-72, Aug. 2015, doi: [10.1109/MMM.2015.2431236](https://doi.org/10.1109/MMM.2015.2431236).
- [24] K. Hashimoto, *Surface acoustic wave devices in telecommunications: Modelling and simulation*. Berlin; New York: Springer, 2000.
- [25] R. Vetry, M. D. Hodge, and J. B. Shealy, "High power, wideband single crystal XBAW technology for sub-6 GHz micro RF filter applications," in *Proc. IUS*, Kobe, Japan, 2018, pp. 206-212, doi: [10.1109/ULTSYM.2018.8580045](https://doi.org/10.1109/ULTSYM.2018.8580045).
- [26] K. Hashimoto, *RF Bulk acoustic wave filters for communications*. Norwood, Mass.: Artech House, 2009.
- [27] M. AlJoumayly, R. Rothmund, M. Schaefer, and W. Heeren, "5G BAW technology: Challenges and solutions," in *Proc. WAMICON*, Clearwater, FL, USA, 2022, pp. 1-3, doi: [10.1109/WAMICON53991.2022.9786171](https://doi.org/10.1109/WAMICON53991.2022.9786171).
- [28] Z. Schaffer, P. Simeoni and G. Piazza, "33 GHz overmoded bulk acoustic resonator," *IEEE Microw. Wirel. Compon. Lett.*, vol. 32, no. 6, pp. 656-659, June 2022, doi: [10.1109/LMWC.2022.3166682](https://doi.org/10.1109/LMWC.2022.3166682).
- [29] W. Zhao *et al.*, "15-GHz epitaxial AlN FBARs on SiC substrates," *IEEE Electron Device Lett.*, vol. 44, no. 6, pp. 903-906, June 2023, doi: [10.1109/LED.2023.3268863](https://doi.org/10.1109/LED.2023.3268863).
- [30] M. Park *et al.*, "A 19 GHz all-epitaxial Al<sub>0.8</sub>Sc<sub>0.2</sub>N cascaded FBAR for RF filtering applications," *IEEE Electron Device Lett.*, vol. 45, no. 7, pp. 1341-1344, July 2024, doi: [10.1109/LED.2024.3404477](https://doi.org/10.1109/LED.2024.3404477).
- [31] S. Cho *et al.*, "Millimeter wave thin-film bulk acoustic resonator in sputtered scandium aluminum nitride," *J. Microelectromechanical Syst.*, vol. 32, no. 6, pp. 529-532, Dec. 2023, doi: [10.1109/JMEMS.2023.3321284](https://doi.org/10.1109/JMEMS.2023.3321284).
- [32] Y. Yang, A. Gao, R. Lu, and S. Gong, "5 GHz lithium niobate MEMS resonators with high FoM of 153," in *Proc. MEMS*, Las Vegas, NV, USA, 2017, pp. 942-945, doi: [10.1109/MEMSYS.2017.7863565](https://doi.org/10.1109/MEMSYS.2017.7863565).
- [33] V. Plessky, *et al.*, "5 GHz laterally-excited bulk-wave resonators (XBARs) based on thin platelets of lithium niobate," *Electronics Letters*, vol. 55, no. 2, pp. 98-100, Jan. 2019, doi: [10.1049/el.2018.7297](https://doi.org/10.1049/el.2018.7297).
- [34] R. Lu, *et al.*, "Multimeter-wave acoustic resonators," U.S. Patent 0 062 738, Feb. 10, 2025.
- [35] R. Lu, "Recent advances in high-performance millimeter-Wave acoustic resonators and filters using thin-film lithium niobate," *Prog. Quantum Electron.*, vol. 100-101, p. 100565, May 2025, doi: [10.1016/j.pquantelec.2025.100565](https://doi.org/10.1016/j.pquantelec.2025.100565).
- [36] R. Lu, Y. Yang, S. Link, and S. Gong, "Al resonators in 128° Y-cut lithium niobate with electromechanical coupling of 46.4%," *J. Microelectromechanical Syst.*, vol. 29, no. 3, pp. 313-319, June 2020, doi: [10.1109/JMEMS.2020.2982775](https://doi.org/10.1109/JMEMS.2020.2982775).
- [37] O. Barrera, S. Cho, J. Kramer, V. Chulukhadze, J. Campbell, and R. Lu, "38.7 GHz thin film lithium niobate acoustic filter," in *Proc. IMFW*, Cocoa Beach, FL, USA, 2024, pp. 87-90, doi: [10.1109/IMFW59690.2024.10477121](https://doi.org/10.1109/IMFW59690.2024.10477121).
- [38] O. Barrera *et al.*, "Thin-film lithium niobate acoustic filter at 23.5 GHz with 2.38 dB IL and 18.2% FBW," *J. Microelectromechanical Syst.*, vol. 32, no. 6, pp. 622-625, Dec. 2023, doi: [10.1109/JMEMS.2023.3314666](https://doi.org/10.1109/JMEMS.2023.3314666).
- [39] O. Barrera *et al.*, "Transferred thin film lithium niobate as millimeter wave acoustic filter platforms," in *Proc. MEMS*, Austin, TX, USA, 2024, pp. 23-26, doi: [10.1109/MEMS58180.2024.10439593](https://doi.org/10.1109/MEMS58180.2024.10439593).
- [40] L. Gao, Y. Yang, and S. Gong, "Wideband hybrid monolithic lithium niobate acoustic filter in the K-Band," *IEEE Trans. Ultrason. Ferroelectr. Freq. Control.*, vol. 68, no. 4, pp. 1408-1417, April 2021, doi: [10.1109/TUFFC.2020.3035123](https://doi.org/10.1109/TUFFC.2020.3035123).
- [41] A. Kochhar *et al.*, "X-band bulk acoustic wave resonator (XBAW) using periodically polarized piezoelectric films (P3F)," in *Proc. IUS*, Montreal, QC, Canada, 2023, pp. 1-4, doi: [10.1109/IUS51837.2023.10306825](https://doi.org/10.1109/IUS51837.2023.10306825).
- [42] S. Cho *et al.*, "23.8-GHz acoustic filter in periodically poled piezoelectric film lithium niobate with 1.52-dB IL and 19.4% FBW," *IEEE Microw. Wirel. Technol. Lett.*, vol. 34, no. 4, pp. 391-394, April 2024, doi: [10.1109/LMWT.2024.3368354](https://doi.org/10.1109/LMWT.2024.3368354).
- [43] Izhar *et al.*, "Periodically poled aluminum scandium nitride bulk acoustic wave resonators and filters for communications in the 6G era," *Microsyst. Nanoeng.*, vol. 11, no. 1, Jan. 2025, doi: [10.1038/s41378-024-00857-4](https://doi.org/10.1038/s41378-024-00857-4).
- [44] IEEE Standard on Piezoelectricity, *ANSI/IEEE, 176-1987*, 1988.
- [45] J. D. Larson, P. D. Bradley, S. Wartenberg, and R. C. Ruby, "Modified Butterworth-Van Dyke circuit for FBAR resonators and automated measurement system," in *Proc. IUS*, San Juan, PR, USA, 2000, pp. 863-868 vol.1, doi: [10.1109/ULTSYM.2000.922679](https://doi.org/10.1109/ULTSYM.2000.922679).
- [46] R. Lu and S. Gong, "RF acoustic microsystems based on suspended lithium niobate thin films: advances and outlook," *J. Micromech. Microeng.*, vol. 31, no. 11, p. 114001, Sep. 2021, doi: [10.1088/1361-6439/ac288f](https://doi.org/10.1088/1361-6439/ac288f).
- [47] K. Shibayama, K. Yamanouchi, H. Sato, and T. Meguro, "Optimum cut for rotated Y-cut LiNbO<sub>3</sub> crystal used as the substrate of acoustic-surface-wave filters," *Proc. IEEE*, vol. 64, no. 5, pp. 595-597, May 1976, doi: [10.1109/PROC.1976.10181](https://doi.org/10.1109/PROC.1976.10181).
- [48] R. S. Weis and T. K. Gaylord, "Lithium niobate: Summary of physical properties and crystal structure," *Appl. Phys. A, Solids Surf.*, vol. 37, no. 4, pp. 191-203, Aug. 1985, doi: [10.1007/BF00614817](https://doi.org/10.1007/BF00614817).
- [49] D. Morgan, *Surface Acoustic Wave Filters*. Amsterdam, The Netherlands: Elsevier, 2007.
- [50] R. Lu, Y. Yang, S. Link and S. Gong, "Low-loss 5-GHz first-order antisymmetric mode acoustic delay lines in thin-film lithium niobate," *IEEE Trans. Microw. Theory Tech.*, vol. 69, no. 1, pp. 541-550, Jan. 2021, doi: [10.1109/TMTT.2020.3022942](https://doi.org/10.1109/TMTT.2020.3022942).
- [51] V. Chulukhadze *et al.*, "Frequency scaling millimeter wave acoustic resonators using ion beam trimmed lithium niobate," in *Proc. EFTF/IFCS*, Toyama, Japan, 2023, pp. 1-4, doi: [10.1109/EFTF/IFCS57587.2023.10272038](https://doi.org/10.1109/EFTF/IFCS57587.2023.10272038).
- [52] T. Zhang, Y. -W. Chang, O. Barrera, N. Ahmed, J. Kramer, and R. Lu, "Acoustic and electromagnetic co-modeling of piezoelectric devices at millimeter wave," *J. Microelectromechanical Syst.*, vol. 33, no. 5, pp. 640-645, Oct. 2024, doi: [10.1109/JMEMS.2024.3431576](https://doi.org/10.1109/JMEMS.2024.3431576).





**TARAN ANUSORN** (Student member, IEEE) received the B.Eng. degree (Hons.) in electrical engineering from Chulalongkorn University, Bangkok, Thailand, in 2023. He is currently a graduate student in electrical and computer engineering at the University of Texas at Austin, Austin, TX, USA.

He has a broad research interest in microwave theory and techniques for next-generation communication and sensing applications, spanning both component and system levels, including RF front-end solutions, miniaturized microwave components, 3D-printable devices, RF MEMS, and RF photonic devices and microsystems. He is a recipient of Anandamahidol Foundation Scholarship, awarded under Thai royal patronage.



**OMAR BARRERA** (Student member, IEEE) Omar is a Ph.D. candidate at UT ECE. He graduated with a B.S. degree from UABC in Mexico and an M.Eng. from Dongguk University in Korea, both in Electrical Engineering. His current research interests involve microwave and mm-wave devices and

circuits, and specifically, acoustic filters for new radio mobile applications. Omar was the recipient of an Outstanding Student Oral Presentation Award Finalist in IEEE MEMS 2024 and was awarded 2nd place in the Conference Paper Award in IEEE IMFW 2024. He has also received the Cadence Diversity in Technology Scholarship in 2023.



**JACK KRAMER** (Student member, IEEE) received his B.S. from the University of New Mexico in 2021 and is currently pursuing his Ph.D. in electrical engineering at the University of Texas at Austin. His research has focused on millimeter-wave and sub-terahertz acoustic systems leveraging lithium niobate thin films, as well as further integration of these systems into hybrid

optical and quantum systems. He received the best student paper awards at IEEE International Frequency Control Symposium (IFCS) 2023 and IEEE International Conference on Microwave Acoustics and Mechanics (IC-MAM) 2022. He also received the 2024 Ben Streetman Junior Researcher Award, the 2025 University of Texas Continuing Fellowship, and the 2025 Texas Quantum Institute Fellowship.



**IAN ANDERSON** (Student member, IEEE) received the B.S. degree in Electrical and Computer Engineering from the Ohio State University, Columbus, OH, USA, in 2023. He is currently a PhD student in Electrical and Computer Engineering at the University of Texas at

Austin, Austin, TX, USA. His current work focuses on design and fabrication of thin film bulk acoustic resonators for infrared

sensors, and work on high frequency phononic combs. He also has further research interests and projects in solidly mounted acoustic devices and acousto-optic modulators. He is a recipient of the NASA Space Technology Graduate Research Opportunity (NSTGRO) Fellowship.



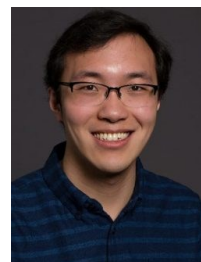
**ZIQIAN YAO** (Student member, IEEE) received the B.S. degree in Electrical Engineering from the University of Wisconsin at Madison, Madison, WI, USA, in 2024. He is currently a PhD student in Electrical and Computer Engineering at the University of Texas at Austin, Austin, TX, USA. His current research focuses on thin-film bulk acoustic

resonator (FBAR), piezoelectric power conversion, and piezoelectric micromachined ultrasonic transducers (PMUT). He is a recipient of UT Graduate School Mentoring Fellowship as well as Cockrell School of Engineering Fellowship.



**VAKHTANG CHULUKHADZE** (Student member, IEEE) received his B.S. from the University of Rochester in 2022 and is currently pursuing his Ph.D. in electrical engineering at the University of Texas at Austin. His research has focused on lithium niobate microsystems spanning a wide range of frequencies and applications, toward front-end signal processing and sensing applications.

Vakhtang is a Jim and Dorothy Doyle scholar, as well as a Russel F. Brand Engineering Acoustics fellow, and a Professor Edith Clarke fellow. He received an outstanding poster award at the Hilton Head workshop 2024 alongside the 2024 Ben Streetman award in graduate research on electronic and photonic devices.



**RUOCHEN LU** (Senior Member, IEEE) is an Assistant Professor in the Department of Electrical and Computer Engineering at The University of Texas at Austin. He received the B.E. degree with honors in microelectronics from Tsinghua University, Beijing, China, in 2014, and the Ph.D. degree in electrical engineering from the University of Illinois at Urbana-Champaign, Urbana, IL, USA, in 2019. His research focuses on

developing chip-scale acoustic and electromagnetic components and microsystems for RF applications. He received IEEE TC-S Microwave Award in 2022, IEEE Ultrasonics Early Career Investigator Award in 2024, and NSF Career Award in 2024. He received the Junior Faculty Excellence in Teaching Award in 2024. He is an associate editor of IEEE Journal of Microelectromechanical Systems, IEEE Transactions on Ultrasonics, Ferroelectrics, and Frequency Control, and a topic editor of IEEE Journal of Microwaves.